Supplementary Material

1) Vessel phantom fabrication

Two molds were designed in Autodesk inventor (Autodesk, San Rafael, CA, USA) and 3-D printed (MakerBot, New York, NY, USA) in order to create a straight vessel phantom, and a phantom mimicking an atherosclerotic vessel with approximately 50% stenosis, similarly as in [1]. The length, inner diameter and wall thickness of the phantoms were 200 mm, 8 mm and 2 mm, respectively. In the case of the stenotic phantom, an ellipsoidal inclusion with 15 mm length was designed 78 mm away from one end of the phantom, in order to mimic the geometry of an atherosclerotic vessel with approximately 50% maximum reduction of luminal area. A polyvinyl alcohol (PVA) mixture was formed by mixing distilled water, PVA powder (Sigma-Aldrich, St. Louis, MO, USA), glycerol and graphite acoustic scatterers (Sigma-Aldrich, St. Louis, MO, USA) at concentrations of 78%, 10%, 10% and 3%, respectively, heated at 90 °C for approximately 40 minutes. Subsequently, the mixture was cooled and then poured inside the 3-D printed mold, and was then subjected to three cycles of freezing (12 h at –20 °C) and thawing (12 h at room temperature). The resulting elastic phantom was then placed inside a custom designed container, and its two ends were connected to plastic fittings. The container was filled with porcine-skin gelatin (Sigma-Aldrich, St. Louis, MO, USA), to serve as the vessel phantom's surrounding medium.

2) Simulations

FSI simulations were carried out similarly as in [1], using the software suite FEBio [2][3]. The 3-D CAD models of the phantom geometries were converted to FE model using Abaqus CAE (v6.13, Dassault Systèmes). The models were separated into a fluid space, which corresponded to the phantom lumen, and a solid space, which included the arterial wall and the gelatin surrounding medium. In the case of the stenotic phantom, the mesh was generated by employing a combination of quadratic tetrahedral (10-node) and pentahedral (15-node) elements using an adaptive meshing algorithm. In the case of the straight phantom, a dense mesh was generated in the lumen area at a distance within 1 mm from the wall, with a node-to-node axial distance equal to 0.05 mm. Appropriate boundary conditions were applied to restrict the motion on the outer surfaces of the surrounding material and the outer surface of the inlet and outlet sections of the arterial model. In addition, zero-fluid velocity was set as boundary condition at the outermost surface of the lumen. The same flow waveform as the one generated by the programmable pump, was imposed at the inlet of the phantom model. The pressure waveform measured by a pressure catheter was imposed at the outlet of the phantom in order to approximate the experimental conditions. A slightly compressible Newtonian viscous fluid was used to simulate the blood mimicking liquid [4] used for the phantom experiments with a mass density, shear viscosity and bulk modulus of 1060 kg/m^3, 4 mPa s and 2 GPa, respectively. The phantom wall was simulated as a homogenous isotropic nearly-incompressible quasilinear viscoelastic material, while the surrounding gelatin was approximated as a homogenous isotropic compressible quasilinear viscoelastic material with a neo-Hookean elastic response. Parameters involving the structural properties of the PVA and surrounding gelatin materials (i.e. elastic constants, viscoelastic coefficients) were experimentally determined. A complete description of the structure part of the simulation can be found in [1]. The simulated fluid shear stress field at each node on the central 2-D slice of the phantom lumen were exported and then post-processed in MATLAB 2017b (Mathworks Inc, Natick, MA, USA). Subsequently, the simulated fluid shear stress was spatially registered with the ultrasound scanning site by using the inlet of the phantom as a reference. Interpolation was performed, in order to map the simulations and ultrasound images at the same grid of size 128 and 80 samples along the lateral (x-axis) and axial (y-axis) directions, respectively. The simulated fluid shear stress at a distance close to the wall that provided optimal approximation of the measured WSS was extracted, and used as the gold standard for the performance assessment.

3) Atherosclerotic swine study

All procedures in this study were approved by the Institutional Animal Care and Use Committee (IACUC) of Columbia University (protocol AC-AAAU6460). Six 3-months old female Wisconsin Mini Swine-Familial Hypercholesterolemic (WMS-FH^{TM}) were acquired from the University of Wisconsin Swine Research Farm (Madison, WI, USA). The animals were fed a high fat diet consisting of 15% lard and 1.2% cholesterol[5]. Surgical intervention was carried out at the baseline of the experiment, in order to ligate the left carotid artery of each animal and accelerate atherosclerosis progression[5]. On the day of the surgery, anesthesia of the animals was induced with intravenous propofol. The animals were intubated and maintained under anesthesia for the procedure using 1 to 2% isoflurane. The throat area was incised on a 5-cm length, in the middle region to access and dissect the left common carotid. A 1.7 mm spacer (a 5F feeding tube/urethral catheter) was placed along the artery before tying it off with 5-0 Prolene (Ethicon, Cornelia, GA, USA). The spacer was then removed, creating an artificial stenosis. Finally, the neck wound was closed and the location of the ligation was indicated externally by a different suture. To estimate the

growth of the artery throughout the study, two tattoo markers were placed at a known distance on the skin right above the carotid arteries, in three pigs, immediately after performing ligation. The increase in the distance between the markers was measured at each scanning time-point.

All animals were euthanized upon completion of the study with an intravenous bolus (100 mg per kg) of euthanasia solution. After euthanasia, an incision was performed in the neck of the animals and the common carotids were extracted, ensuring the whole region imaged in the ultrasound acquisitions was included. The extracted carotids were fixed in 10% formalin according to the following procedure. The distal end of the carotid was closed with a suture, a syringe filled with formalin was introduced and tied with a suture, at the proximal end. Formalin was injected and the pressure was maintained for 5 minutes. The carotids were then stored in a solution of 10% formalin for at least 48 h to allow complete fixation of the tissue. The left atherosclerotic carotid was cut in a series of 5 mm segments, using the site of initial ligation as a reference. The contralateral carotid being more homogeneous, only three 5 mm segments were cut for histology analysis. These segments were placed in a solution of 70% ethanol before being embedded in paraffin. Two 5 μm slices were cut from each segment: one was stained with hematoxy- lineosin, and another was stained with Masson's trichrome to determine the presence of atherosclerotic lesions. To spatially register the histology slices with their approximate location in the ultrasound images, a correction factor was applied, accounting for the in-vivo stretch of common carotid arteries in pigs as reported in [6] and the growth of the animals during the study based on the distance between the tattoo markers. By using the correction factor, it was determined that the 5 mm regions corresponded to segments of approximately 5.4 mm in the ultrasound field of view.

4) Comparison with conventional WSS estimation

In this section, the performance of the proposed adaptive WSS imaging technique is compared with two conventional WSS calculation methodologies, in the case of the straight vessel phantom experiments and a non-ligated swine carotid artery in-vivo.

The first method approximates WSS by using a single velocity at a fixed distance (SVFD) as follows:

$$\text{WSS}_{\text{SVDF}} = \mu * \left. \frac{v_t(r)}{r} \right|_{r=r_{wall}} \quad (S1)$$

Where μ denotes the fluid viscosity and $v_t(r)$ is the tangent flow velocity component with respect to the distance from the wall, r. WSS_{SVDF} was calculated using two different values for r_{wall}: 1) For r_{wall}=1 mm, as reported in [7]. 2) For r_{wall}=0.5 mm, which was the distance that provided optimal agreement between WSS_{SVDF} and simulated WSS. The second conventional approach derives WSS by calculating the mean velocity within a fixed distance (MVFD), as follows [8]:

$$\text{WSS}_{\text{MVDF}} = \mu * \sum_{r=dr}^{r_{wall}} \frac{v_t(r)}{r} \quad (S2)$$

Where r_{wall} was set at 1 mm and dr denotes the spacing between adjacent flow velocity measurements which is equal to 0.01848 mm. The repeatability and accuracy of each WSS calculation methodology were evaluated by calculating the average relative standard error of the means, $\widehat{\text{SEM}}_r(\%)$, and relative error, $\widehat{E_r}$ (%), similarly as in section II-G.

The solid black lines in figure S1-A), B) demonstrate the average value of peak systolic (PS) and end diastolic (ED) WSS_{SVDF}, respectively, with respect to the lateral position for r_{wall}=1 mm. The error bars denote the standard error of the means among different measurements (N=12). The red solid lines show the corresponding values, $\text{WSS}_{PS}^{sim}(x)$ and $\text{WSS}_{ED}^{sim}(x)$, as obtained through simulations. Figure S1-C),D) illustrate the respective PS and ED values for WSS_{SVDF} calculated at r_{wall}=0.5 mm. Figure S1-E),F) demonstrate the respective PS and ED plots for WSS_{MVDF}. Table I summarizes the $\widehat{\text{SEM}}_r(\%)$ and $\widehat{E_r}$ (%) obtained through the proposed adaptive WSS imaging technique and the conventional WSS measurements. It can be observed that in most cases, the adaptive approach provided lower $\widehat{\text{SEM}}_r(\%)$ and $\widehat{E_r}$ (%) as compared to the conventional techniques. WSS_{SVDF} for r_{wall}=0.5 mm provided smaller $E_r(\%)$ in the case of the end diastole, indicating that the proposed adaptive WSS technique is particularly robust at higher flow velocity magnitudes.
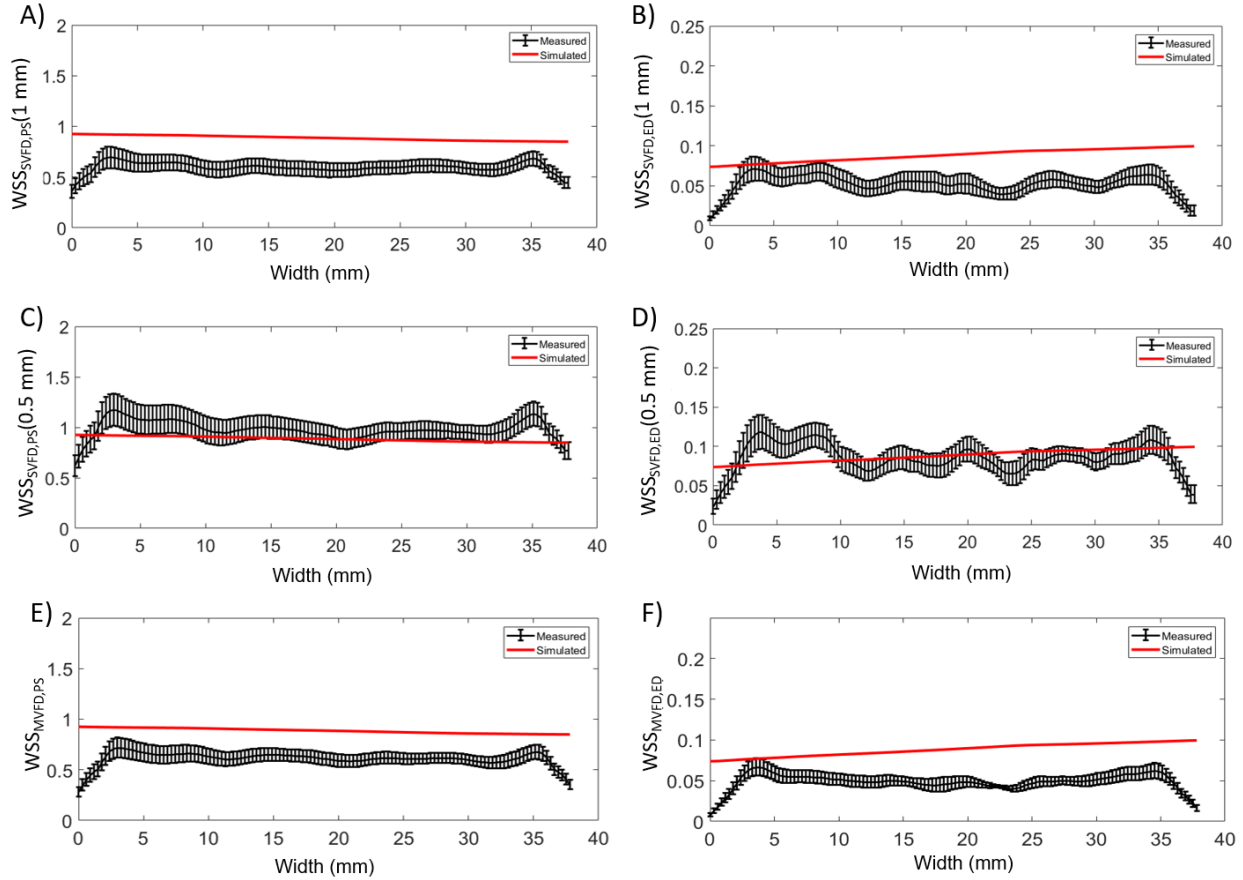
Figure S1: A, B) Average value of peak systolic (PS) and end diastolic (ED) WSS_{SVDF}, respectively, with respect to the lateral position for $r_{wall}=1$ mm. The error bars denote the standard error of the means among different measurements (N=12). The red solid lines show the corresponding values, $WSS_{PS}^{sim}(x)$ and $WSS_{ED}^{sim}(x)$, as obtained through simulations. C),D) PS and ED values for WSS_{SVDF} calculated at $r_{wall}=0.5$ mm. E),F) PS and ED values for WSS_{MVDF}.

TABLE I: $\widehat{SEM}_r(\%)$, and relative error, $\widehat{E}_r$ (%) for different WSS imaging approaches.

Technique	$\widehat{SEM}_{r,PS}(\%)$	$\widehat{E}_{r,PS}$ (%)	$\widehat{SEM}_{r,ED}(\%)$	$\widehat{E}_{r,ED}$ (%)
$WSS_{adaptive}$	6.9	6.7	10.9	19.8
WSS_{SVDF} (1 mm)	11.9	32.0	19.7	37.9
WSS_{SVDF} (0.5 mm)	11.1	12.2	17.4	16.5
WSS_{MVDF}	9.9	29.8	13.7	39.4

In addition, the performance of the proposed adaptive WSS imaging technique was evaluated against conventional methods in a non-ligated artery of a healthy swine at Day 0 of the experiment. Given the absence of gold-standard theoretical WSS values, we assess the $\widehat{SEM}_r(\%)$ for N=5 repetitions of the WSS methodology processing steps corresponding to the same ultrasound acquisition. Manual steps such as arterial wall segmentation were carried out by a different operator for each repetition, who was blinded to the study results. Figure 1-A) demonstrates the combined PWI and VFI imaging sequence in a non-ligated swine carotid artery. The vector flow field and arterial wall displacements are color-coded and overlaid onto the B-mode image. Figure 1-B),C) and D) show the mean value and SEM of WSS_{PS} among N=5 processing repetitions obtained through the adaptive, SVFD and MVFD techniques, respectively. It can be observed that the error bars indicate very small variation in the case of adaptive WSS imaging in Figure 1-B), as compared to Figure 2-C) and D). A lower $\widehat{SEM}_{r,PS}(\%)$ was observed in the case of the adaptive technique (0.8 %), as compared to SVFD (5.3 %) and MVFD (9.9 %). Those results suggest that the adaptive technique is less affected by the wall segmentation. This can be attributed to the fact that the adaptive technique identifies and adapts the distance for WSS calculation in the same region with most uniform slope, regardless of the segmentation lines. On the contrary, SVFD and MVFD are more dependent on the segmentation,

given that different positioning of the segmentation lines, combined with the use of a fixed distance, will result in different regions of WSS estimation.
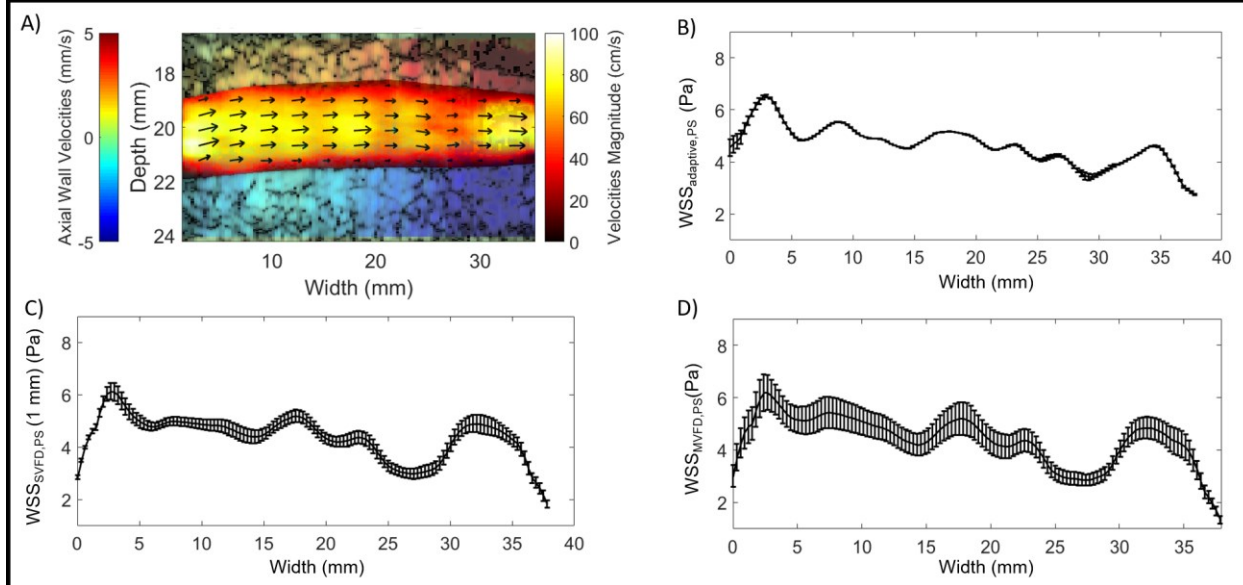

Figure S2: A) Combined PWI and VFI map in a non-ligated swine carotid artery. B),C),D) mean value and SEM of WSS_{PS} among N=5 processing repetitions obtained through the adaptive, SVFD and MVFD techniques for WSS calculation, respectively.

5) Singular value decomposition clutter filter

A singular value decomposition (SVD) filtering approach was employed to filter out RF signals corresponding to tissue as described in [9]. Let us consider a 3-D stack of beamformed RF frames with size (M_y, M_x, M_t), where M_z, M_x, M_t denote the number of samples across the depth, width and time axes, respectively. The first step of the employed filtering approach is reshaping the 3-D stack to a 2-D Casorati matrix (S) of dimension $(M_x \times M_y, M_t)$. In turn, S is diagonalized and decomposed into a temporal (U) and spatial (V) singular vector basis:

$$S = U \Delta V^*$$

Where the diagonal matrix Δ includes the singular values of S.

Singular values characterized by high energy correspond to stationary and slow moving tissue signals with high spatiotemporal coherence. Therefore, the aim is to reject components with high energy singular values based on a threshold, δ_T. To select the threshold, the singular values of Δ are sorted in descending order, forming the curve shown in Figure 1-A). The threshold δ_T that provides separation between tissue motion (high singular values) and blood flow or noise (low singular values) is chosen as the first elbow of the curve, as illustrated in red vertical line in Figure 1-A).

Figure 1-B) demonstrates an example flow velocity profile when the singular value shown in figure 1-A) is selected. Figure 1-C,D) demonstrate a threshold selection corresponding to a higher number of singular value and the resulting flow velocity profile. It can be observed that different choices for δ_T, provide different flow velocity profiles, which would result in different WSS values. This example highlights the importance of using consistent criteria, such as the elbow method for δ_T selection, in order to obtain robust and consistent flow velocity and WSS values.
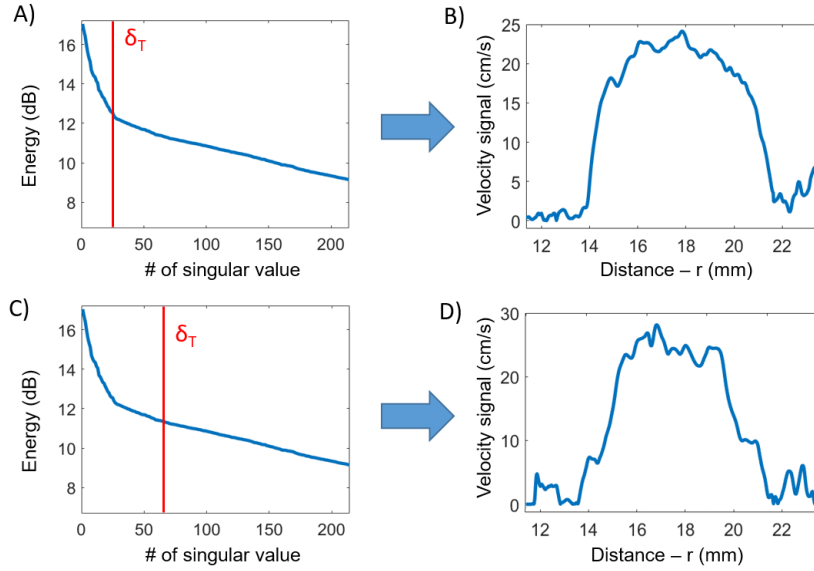
Figure 2: Effect of clutter filter threshold selection on estimated flow velocity profile.

6) Effect of low stenotic plaque in WSS estimation

In the case of the human study, global peak systolic WSS values ($WSS_{ps,g}$) are compared between non-pathological, and atherosclerotic carotid arteries presenting low stenotic plaques (<40% stenosis). In this section, we quantify the effect of low stenotic plaque geometry and plaque stiffness in $WSS_{ps,g}$ values. A model of a vessel phantom mimicking an atherosclerotic vessel with 30% stenosis was developed, as described in section 2 of the supplemental material. Two FSI simulations were carried out, similarly as in section II-D, by assigning different stiffness values to the material simulating the stenotic segment: 1) Plaque with the same stiffness as the wall (42.2 kPa) and 2) Plaque three times stiffer than the wall (126.6 kPa).

Figure 3 demonstrates the result of the FSI simulation, where the color-map demonstrates the fluid shear stress values in the central 2-D slice of the 3-D model. For each simulation, $WSS_{ps,g}$ was calculated at two sites: 1) in a pre-stenotic straight segment and 2) a stenotic segment with the plaque in the field of view (FOV). The same FOV as in the case of ultrasound acquisitions was employed which was equal to 37.8 mm. The $WSS_{ps,g}$ was equal to 0.78 Pa, 0.85 Pa and 0.87 Pa in the case of the straight segment, the stenotic segment with the softer plaque, and the stenotic segment with the stiffer plaque, respectively. Therefore, the presence of a low stenotic plaque with the same stiffness as the wall elevated $WSS_{sp,g}$ by 8,9%, as compared to the straight phantom segment, while the stiffer plaque caused a slight $WSS_{sp,g}$ elevation, which was equal to 2.3% relative to the softer plaque.
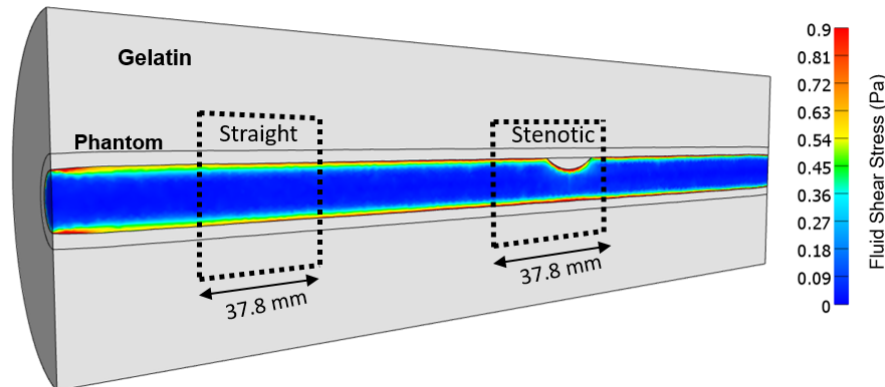

Figure 3: Simulated fluid shear stress in a vessel phantom presenting approximately 30% stenosis.

[1]   G. Vittorio, P. Nauleau, G. M. Karageorgos, J. Shim, G. Ateshian, and E. Konofagou, "Modelling pulse wave propagation through a stenotic artery with fluid structure interaction: a validation study using ultrasound pulse wave imaging," *Biomech. Model. Mechanobiol.*

[2]   S. A. Maas, B. J. Ellis, G. A. Ateshian, and J. A. Weiss, "FEBio: Finite Elements for Biomechanics," *J. Biomech. Eng.*, vol. 134, no. 1, Feb. 2012.

[3]   G. A. Ateshian, J. J. Shim, S. A. Maas, and J. A. Weiss, "Finite Element Framework for Computational Fluid Dynamics in FEBio," *J. Biomech. Eng.*, vol. 140, no. 2, p. 0210011, Feb. 2018.

[4]   K. V Ramnarine, D. K. Nassiri, P. R. Hoskins, and J. Lubbers, "Validation of a New Blood-Mimicking Fluid for Use in Doppler Flow Test Objects," *Ultrasound Med. Biol.*, vol. 24, no. 3, pp. 451–459, Mar. 1998.

[5]   A. Ishii *et al.*, "Swine Model of Carotid Artery Atherosclerosis: Experimental Induction by Surgical Partial Ligation and Dietary Hypercholesterolemia."

[6]   H.-C. Han and D. N. Ku, "Contractile Responses in Arteries Subjected to Hypertensive Pressure in Seven-Day Organ Culture," 2001.

[7]   V. Perrot *et al.*, "Translation of Simultaneous Vessel Wall Motion and Vectorial Blood Flow Imaging in Healthy and Diseased Carotids to the Clinic: A Pilot Study," *IEEE Trans. Ultrason. Ferroelectr. Freq. Control*, vol. 68, no. 3, pp. 558–569, Mar. 2021.

[8]   Y. Du *et al.*, "Wall Shear Stress Measurements Based on Ultrasound Vector Flow Imaging: Theoretical Studies and Clinical Examples," *J. Ultrasound Med.*, vol. 39, no. 8, pp. 1649–1664, Aug. 2020.

[9]   G. M. Karageorgos *et al.*, "Pulse wave imaging coupled with vector flow mapping: A phantom, simulation and in vivo study," *IEEE Trans. Ultrason. Ferroelectr. Freq. Control*, pp. 1–1, 2021.